Summary and Conclusions

The studies presented in this thesis cover the most energetic light emitted by pulsars and pulsar wind nebulae. Both source types are known to emit gamma rays in the very-high-energy (VHE) range and have been detected by Imaging Atmospheric Cherenkov Telescopes (IACTs) from the ground. For our studies we mainly used data from the Major Atmospheric Gamma-ray Imaging Cherenkov (MAGIC) telescopes, one of the current three major IACTs in the world. We also analyzed data from the Large Area Telescope (LAT) on board of the *Fermi* satellite, which owing to its wide field of view and overlapping energy range, is perfectly suited to provide observational guidance to IACTs.

The main result of this work is the discovery of pulsed emission from the Crab pulsar up to $\sim$1.2 TeV, the most energetic light ever seen from this class of astrophysical objects. This achievement was rendered possible by an unprecedented large data set of $\sim$414 h from the MAGIC telescopes (see Chap. 5). We were able to detect the inter-pulse P2 in the Crab pulsar's phaseogram at a 5.2σ level above 400 GeV and derived a steep power-law like spectrum with a photon index of 3.13 ± 0.18 in a broad energy range from $\sim$85 GeV to $\sim$1.2 TeV. The main pulse P1, on the other hand, is barely visible at energies above 400 GeV and we could only determine its spectrum up to $\sim$500 GeV. Both peak spectra connect smoothly to the *Fermi*-LAT spectral points above 10 GeV. Joint power-law fits to the MAGIC and *Fermi*-LAT spectral points revealed a significant difference between the photon indexes of the main pulse P1 (3.54 ± 0.09) and the inter-pulse P2 (3.01 ± 0.06). This sustains the trend of a decreasing intensity ratio $P1/P2$ with energy, as seen by the *Fermi* LAT above 1 GeV, and extrapolates this tendency into the TeV regime.

These results lead to several implications for the emission model of the Crab pulsar. Gamma rays with energies of $\sim$1 TeV must be produced at least $\sim$600 km away from the neutron star to be able to escape the pulsar's magnetosphere, which challenges some of the *slot gap* and *annular gap* models. Regarding the emission mechanism, it seems highly unlikely that pulsed TeV photons are produced via synchro-curvature radiation, which is the standard emission mechanism for gamma-ray pulsars in the GeV regime, since it would require unusual large curvature radii.

D. Carreto Fidalgo, *Revealing the Most Energetic Light from Pulsars and Their Nebulae*, Springer Theses, https://doi.org/10.1007/978-3-030-24194-0

A more plausible mechanism is inverse Compton scattering, which was already put forward after the detection of the >100 GeV pulsation by VERITAS and MAGIC in 2012. Assuming inverse Compton scattering in the Klein-Nishina limit, the Lorentz factors of the accelerated electrons have to be greater than $\sim 2 \times 10^6$ to produce 1 TeV photons. Two models by Aleksić et al. [1, based on the work by Kouichi Hirotani] and [2], among many other models, tried to explain the pulsed emission up to 400 GeV from the Crab pulsar. We discussed both models in the context of the newly found TeV emission and showed that substantial modifications would be necessary in the case of Aharonian et al. [2]. Open questions that have yet to be addressed by theoretical models are the narrow peaks observed in the pulse profile above 100 GeV, the decreasing intensity ratio $P1/P2$ with energy and the phase coherence of the peaks along the entire electromagnetical spectrum, from radio up to TeV energies.

The observation of pulsed TeV photons provides a unique set of data to investigate fundamental physics. In Chap. 6 we used our large data set of the Crab pulsar to test for Lorentz Invariance Violation (LIV) in terms of a wavelength dependent speed of light. For this purpose we modeled the gamma-ray emission of the inter-pulse incorporating an energy dependent (linearly or quadratically) group velocity of photons for a *subluminal* and *superluminal* scenario. By applying Bayesian inference to obtain our model parameters, we were able to derive conservative 95% lower limits on the invariant energy scales, assuming either a linear or quadratic energy dependence. Our quadratic limits $E_{QG_2} > 3.1 \times 10^{10}$ GeV and $E_{QG_2} > 1.6 \times 10^{10}$ GeV, for a subluminal and superluminal scenario, respectively, corroborate the principle findings by Ahnen et al. [3] and are a factor of $\lesssim$6 worse than the current world-best limits. They show, however, much room for improvement considering the upcoming Cherenkov Telescope Array (CTA) observatory.

While over 200 pulsars are known to emit gamma rays in the MeV to GeV regime, only two pulsars have been detected in the VHE range to date: the Crab and the Vela pulsar. Against this background, in Chap. 7 we conducted a search for a possible next very-high-energy pulsar looking through the wealth of gamma-ray pulsars discovered by *Fermi*-LAT. Since we wanted to make use of the pulsars' timing information in our search, we restricted ourselves to millisecond pulsars (MSPs), which are easier to time compared to canonical pulsars. We focused on MSPs that would be well observable from the MAGIC site, and further included Geminga and PSR J0614- 3329 to our sample, two known and promising candidates for VHE emission. Using almost 90 months of *Fermi*-LAT data, we found evidence for >50 GeV pulsation from the MSP PSR J0614- 3329, which seems to be a compelling candidate for follow-up observations by IACTs in the Southern Hemisphere.

In Part III of this thesis we put aside VHE emission from pulsars and focused on TeV emission from pulsar wind nebulae (PWNe). Motivated by a Milagro hot spot (3.7σ) at ~35 TeV, we conducted observations in the direction of the young and energetic gamma-ray pulsar PSR J0631+1036 with the MAGIC telescopes to look for steady TeV emission from a possibly extended PWN around the pulsar. We collected a total amount of ~37 h of high quality data, but found no hint of a signal in our analysis. 95% confidence upper limits on the integral flux F_{300} above

300 GeV were computed assuming a photon index of 2.2 and under the assumption of a point-like emission ($F_{300} < 6.0 \times 10^{-13}$ cm^{-2} s^{-1}) and a disk-like emission profile with radius $r_{\rm pwn} = 0.3°$ ($F_{300} < 2.8 \times 10^{-12}$ cm^{-2} s^{-1}). These limits are in tension with Milagro's results and corroborate the non-detection recently reported by HAWC. Putting the limits in the context with the TeV PWN population study by Abdalla et al. [4], we concluded that our luminosity limits for a possible TeV PWN around PSR J0631 lie within the observed scatter of TeV PWN luminosities in our galaxy.

During the course of his Ph.D. studies, the author of this thesis spent several months at the Roque de los Muchachos Observatory in La Palma, Canary Islands (Spain), to carry out observations for the MAGIC collaboration. He also participated in the refinement of the analysis of data taken with a new trigger system and made significant improvements to the on-site analysis (OSA) chain, for which he was one of the persons in charge and which provides the low-level analysis products to the whole collaboration. His contributions supported the scientific output by the MAGIC collaboration, whose results have always made and continue to make a significant impact in the field of VHE astrophysics.

Regarding the future of VHE gamma-ray astronomy, a key player for its progress will be the upcoming Cherenkov Telescope Array (CTA) Observatory. This major project is ran by over 1400 members in 32 countries,[1] and will consist of more than 100 telescopes located in the Northern and Southern Hemisphere providing a nearly full-sky coverage. CTA's sensitivity will outperform current generation IACTs by an order of magnitude and most likely improve many of the results presented in this thesis. With far less observation time, CTA will be able to either measure the Crab pulsar spectrum up to energies far beyond $\sim$1 TeV or detect a cut-off in its VHE tail. This should allow us to stringently limit the LIV energy scales and should provide world-best limits for the quadratic term. Furthermore, the low energy threshold of CTA's Large Size Telescopes (LSTs) of about 25 GeV will presumably increase the number of gamma-ray pulsars detected by IACTs, and thus contribute to a better understanding of the scarce VHE component in pulsars. Concerning pulsar wind nebulae, one of CTA's Key Science Project is the survey of the full Galactic plane. This survey will be a factor of 5–20 more sensitive than current attempts and is expected to add many more members to the population of TeV PWNe, not only towards the Galactic Center but also from the outer part of the galaxy [5]. All in all, CTA seems a promising tool for studying the most energetic light from pulsars and their nebulae.

[1] https://www.cta-observatory.org, last accessed 11/04/2018.

References

1. Aleksić J et al (2012) Phase-resolved energy spectra of the Crab pulsar in the range of 50–400 GeV measured with the MAGIC telescopes. Astron Astrophys 540:A69. https://doi.org/10.1051/0004-6361/201118166
2. Aharonian FA et al (2012) Abrupt acceleration of a 'cold' ultrarelativistic wind from the Crab pulsar. https://doi.org/10.1038/nature10793
3. Ahnen ML et al (2017) Constraining Lorentz invariance violation using the Crab pulsar emission observed up to TeV energies by MAGIC. Astrophys J Suppl Ser 232(1):9. https://doi.org/10.3847/1538-4365/aa8404
4. Abdalla H et al (2018) The population of TeV pulsar wind nebulae in the H.E.S.S. galactic plane survey. Astron Astrophys 612:A2. https://doi.org/10.1051/0004-6361/201629377
5. The Cherenkov Telescope Array Consortium, et al (2017) Science with the Cherenkov Telescope Array

Appendix A
Interaction Processes in Very-High-Energy Astrophysics

Cosmic gamma rays are primarily produced in interactions of charged, energetic cosmic rays (electrons/positrons and protons) with ambient electromagnetic fields or matter. Gamma rays are therefore able to map densities and energetics of cosmic rays as well as their interaction partners, often referred to as "targets". Here we will superficially sketch the most relevant interaction processes for this theses, including the ones relevant for the instrumental detection of very-high-energy (VHE) gamma rays. Detailed treatments can be found in the canonical publications and textbooks by Blumenthal and Gould [1], Rybicki and Lightman [2], Jackson [3], Aharonian [4], Longair [5].

Bremsstrahlung Also referred to as *free-free emission*, Bremsstrahlung is the radiation of an unbound charged particle due to its acceleration in the Coulomb field of another charged particle. The intensity spectrum radiated by a single electron in the field of a nucleus is constant up to a cut-off frequency, at which it decays exponentially. Bremsstrahlung is the dominant energy-loss mechanism for electrons and positrons entering the atmosphere. In the relativistic limit the energy loss rate $-\mathrm{d}E/\mathrm{d}t$ is proportional to E, resulting in the exponential loss of energy by the electron. It is common to define a radiation length X_0 for which the electron looses a fraction $(1 - 1/e)$ of its energy. In astrophysics the bremsstrahlung of a thermal plasma is called *thermal bremsstrahlung* and is primarily observed in the X-ray band from hot intracluster gas in a galaxy cluster.

Synchrotron radiation The motion of a charged particle in a uniform static magnetic field B will generally consist of a constant velocity along the magnetic field lines and a circular motion about it, resulting in a spiral path with constant pitch angle α (see Fig. A.1, left panel). In the non-relativistic case ($v \ll c$), when the beaming of the radiation can be neglected, an electron (charge e) with the mass m_e emits energy at the non-relativistic gyrofrequency $\nu_g = eB/2\pi m_e$ or $\nu_g = 28\,\mathrm{GHz\,T^{-1}}$. In the ultrarelativistic limit ($v/c \approx 1,\ \gamma \gg 1$, where v is the velocity of the charged particle, c the speed of light and γ denotes the Lorentz factor), the Doppler and aberration effects result in a spread of emitted frequencies and the radiation may be regarded as a continuous spectrum. The spectral photon

D. Carreto Fidalgo, *Revealing the Most Energetic Light from Pulsars and Their Nebulae*, Springer Theses, https://doi.org/10.1007/978-3-030-24194-0

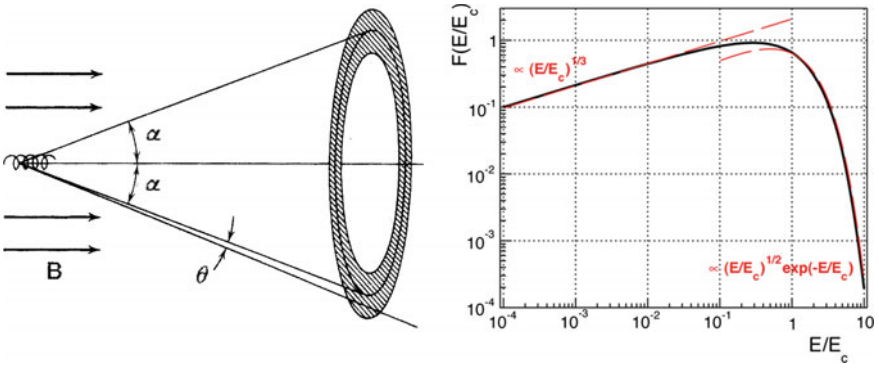

Fig. A.1 Characteristics of synchrotron radiation. **Left**: Trajectory of a charged particle in a uniform static magnetic field with pitch angle α. In the ultrarelativistic limit the radiation is confined to the shaded solid angle ($\theta \propto 1/\gamma$) in the direction of the electron velocity, forming a cone with half-angle α. Figure adopted from [5]. **Right**: The Function $F(x)$, see Eq. A.2, plotted in logarithmic space. E is the energy of the emitted photon by the synchrotron process and E_c a defined critical Energy (see Eq. A.3)

flux per unit time $N(E)$ of a single electron can be written as

$$N(E) = \frac{\sqrt{3}e^3 B \sin\alpha}{4\pi\,\varepsilon_0 c m_e h} F\,(E/E_c)\,, \tag{A.1}$$

$$F(x) = x \int_x^\infty K_{5/3}(z)\mathrm{d}z, \tag{A.2}$$

$$E_c = \frac{3}{2}\gamma^2 h \nu_L \sin\alpha, \tag{A.3}$$

where ε_0 is the electric constant, h the Planck constant and $K_{5/3}$ is the modified Bessel function of order 5/3. E_c is the so-called *critical energy* at which the emission spectrum roughly reaches his maximum ($E_{max} \approx 0.29E_c$). The shape of the spectrum is defined by the function $F(x)$ and is shown in the right panel of Fig. A.1. The asymptotic expressions for function $F(x)$ are

$$F(x) \propto \begin{cases} (E/E_c)^{1/3} & \text{for } E \ll E_c \\ (E/E_c)^{1/2} \exp\left(-E/E_c\right) & \text{for } E \gg E_c, \end{cases} \tag{A.4}$$

indicating an exponential cutoff at energies above E_c. The total energy loss rate is proportional to

$$-\left(\frac{\mathrm{d}E}{\mathrm{d}t}\right) \propto B^2\gamma^2 \sin^2\alpha. \tag{A.5}$$

The time resulting from the division of the electron energy ($E_e = \gamma c m_e^2$) by the total energy loss rate is also known as the *synchrotron cooling time*.
Assuming that the electron energies exhibit a power-law distribution with spectral index p, the spectrum of the synchrotron radiation also follows a power-law with the index $(p-1)/2$ [5].

Curvature radiation In a curved magnetic field, assuming that its curvature is much bigger than the gyroradius, a charged particle will move along the bended magnetic filed lines. Since it will be accelerated transversely, in addition to the synchrotron radiation it will radiate another component called *curvature radiation*. By presuming that the curved trajectory of the particle is due to an introduced virtual magnetic field, and not because of the curved magnetic field lines, one can easily establish an analogy to the closely related synchrotron radiation. In the ultrarelativistic case and adopting a pitch angle of $\sin\alpha = 1$, the gyroradius of an electron is written as $r = \gamma m_e c/eB$. Adopting the analogy illustrated in Fig. A.2, we introduce the virtual magnetic field

$$B_{\mathrm{curv}} = \frac{\gamma m_e c}{r_{\mathrm{curv}} e}, \tag{A.6}$$

r_{curv} being the radius of the curved magnetic field line. Replacing the magnetic field in Eqs. A.1 and A.3 with B_{curv} one obtains the corresponding quantities for the curvature radiation. The critical energy and the energy loss rate in case of curvature radiation are

$$E_{c,\mathrm{curv}} = \frac{3}{2}\hbar c \gamma^3 \frac{1}{r_{\mathrm{curv}}} \quad \text{and} \tag{A.7}$$

$$-\left(\frac{\mathrm{d}E}{\mathrm{d}t}\right)_{\mathrm{curv}} \propto \gamma^4 / r_{\mathrm{curv}}^2. \tag{A.8}$$

The maximum Lorentz factor γ_{max} of an electron emitting curvature radiation, which is continuously being accelerated by an electric field E, is limited by the equilibrium of energy loss rate (see Eq. A.8) and energy gain rate ($\mathrm{d}E/\mathrm{d}t = eEc$),

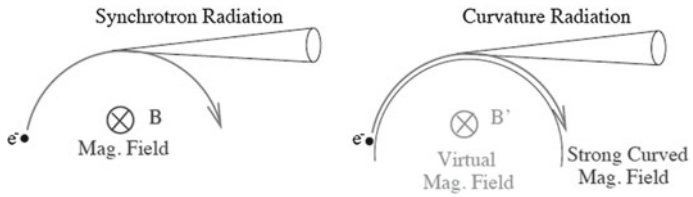

Fig. A.2 Sketch of the analogy between synchrotron and curvature radiation. **Left**: Trajectory for an electron in a magnetic field emitting synchrotron radiation. **Right**: Electron moving along a strong magnetic field line. The trajectory of the electron can be explained by introducing a virtual magnetic field. Figure taken from Saito [6]

$$\gamma_{\max} \propto E^{\frac{1}{4}} \sqrt{r_{\text{curv}}}\,. \tag{A.9}$$

Assuming a power-law spectrum for the electrons' energies with spectral index p, the spectrum of the curvature radiation follows a power-law with the index $(p-2)/3$ [7].

In the most general case, electrons can be accelerated along a curved magnetic field line and spiral around them at the same time. This leads to the formulation of a *synchro-curvature radiation*, for which a detailed summary can be found in the excellent review by Vigano et al. [8]. They introduce a synchro-curvature parameter $\xi = (r_{\text{curv}} \sin^2\alpha)/(r_{\text{gyr}} \cos^2\alpha)$, where r_{gyr} is the relativistic gyroradius. For $\xi \ll 1$, the curvature radiation dominates the emission, if $\xi \gg 1$, synchrotron losses start to dominate.

Inverse Compton scattering In Inverse Compton (IC) scattering, the ultrarelativistic electron scatters a low energy photon ε to higher energies ε' so that the photon gains energy at the expense of the kinetic energy of the electron. The maximum energy transfer occurs for head-on collisions between the electron and the photon. In this scenario we can write the photon energy after the scattering as (see Eq. 2.52 in [1])

$$\varepsilon' = \frac{4\varepsilon\gamma^2 m_e c^2}{m_e c^2 + 4\varepsilon\gamma}, \tag{A.10}$$

where m_e is the rest mass of the electron and γ its Lorentz factor. In the limit of $\gamma\varepsilon \ll m_e c^2$ (also referred to as *Thompson limit*) the maximum scattered photon energy can be written as $\varepsilon' \sim 4\varepsilon\gamma^2$, on the other hand in the *Klein-Nishina limit*, that is $\gamma\varepsilon \gtrsim m_e c^2$, the maximum photon energy is $\varepsilon' \sim \gamma m_e c^2$. In the Thompson limit the electron tends to loose small fractions of its energy in a continuous series of Compton scatterings, while in the Klein-Nishina regime the scattered photon carries away a large part of the electron's energy in a single scattering process. A power-law spectrum of the electrons' energies with spectral index p, results in a power-law energy spectrum of the scattered radiation with index $(p-1)/2$ [5].

The case in which electrons upscatter low energy photons emitted by themselves through synchrotron radiation, is known as *synchrotron-self-Compton* (SCC) radiation.

π^0 decay The most important gamma-ray emission process by hadrons is the decay of a neutral pion into two gamma rays. Neutral pions are mostly produced in inelastic collisions between hadronic cosmic rays (protons or α particles) and have a decay lifetime of only 8.4×10^{-17} s after which they enter the decay channel of $\pi^0 \rightarrow \gamma + \gamma$ with a probability of $\sim$0.99.

The produced high-energy gamma-ray spectrum follows the energy spectrum of the pions and essentially reproduces the spectrum of the parent protons. Very energetic hadronic collisions also produce charged pions with comparable probabilities, which decay into neutrinos. In astrophysics the detection of correlated neutrino and gamma-ray fluxes is therefore a strong indication for hadronic acceleration mechanisms at the emission site.

Pair production For very-high-energy (VHE) photons the pair production process dominates the photon cross section when interacting with matter [9]. Above the energy threshold of $2m_e c^2$, m_e being the rest mass of an electron and c the speed of light, a photon is able to decay into an electron-positron pair ($e^{\pm}$) in the field of a nucleus or an electron ($\gamma \rightarrow e^+ + e^-$). The field is necessary, since one-photon pair production cannot conserve both energy and momentum in field-free space. The cross sections of Bremsstrahlung and pair production are closely related through their similar Feynman diagrams. Therefore, the mean free path of pair production X_p can be expressed by the radiation length of Bremsstrahlung X_0 via $X_p = (9/7)X_0$.

In pulsars the strong magnetic field is able to consume the extra momentum of one-photon pair production and the resulting *magnetic pair creation* is an important absorption mechanism that prevents the escape of gamma rays from the pulsar's magnetosphere. In contrast to one-photon pair production, the mechanism of two-photon pair production also works in a field-free environment. In astrophysics this mechanism explains the attenuation of very-high-energy gamma rays from far away sources through their interaction with the extragalactic background light (EBL, $\gamma_{\mathrm{VHE}} + \gamma_{\mathrm{EBL}} \rightarrow e^+ + e^-$).

Photon splitting One photon can divide in two or more photons with lower energies in the presence of a strong magnetic field. In pulsars the rate of this process is generally much smaller than that of magnetic pair creation above the energy threshold $\varepsilon = 2m_e c^2 / \sin\theta$, where θ is the angle between the magnetic field and the photon's velocity vector [10]. Below the threshold ε, however, it significantly contributes to the absorption of energetic photons from neutron stars magnetospheres.

References

1. Blumenthal GR, Gould RJ (1970) Bremsstrahlung, synchrotron radiation, and compton scattering of high-energy electrons traversing dilute gases. Rev Mod Phys 42(2):237–270. https://doi.org/10.1103/RevModPhys.42.237
2. Rybicki GB, Lightman AP (1979) Radiative processes in astrophysics. Wiley-Interscience, New York (ISBN 0471827592)
3. Jackson JD (1998) Classical electrodynamics, 3rd edn. Wiley, New York (ISBN 047130932X)
4. Aharonian FA (2004) Very high energy cosmic gamma radiation: a crucial window on the extreme universe. World Scientific, Singapore (ISBN 9812561730)
5. Longair MS (2011) High energy astrophysics, 3rd edn. Cambridge University Press, Cambridge (ISBN 0521756189)
6. Saito T (2010) Study of the high energy gamma-ray emission from the Crab pulsar with the MAGIC telescope and Fermi-LAT. PhD thesis, LMU
7. Zhang B, Dai ZG (2011) Synchro-curvature self-compton radiation of electrons in curved magnetic fields. Mon Not R Astron Soc 414(4):2785–2792. https://doi.org/10.1111/j.1365-2966.2010.18187.x
8. Vigano D et al (2014) Compact formulae, dynamics and radiation of charged particles under synchro-curvature losses. Mon Not R Astron Soc 447(2):1164–1172. https://doi.org/10.1093/mnras/stu2456

9. Groom DE, Klein SR (2000) Passage of particles through matter. Euro Phys J C 15(1–4):163–173. https://doi.org/10.1007/BF02683419
10. Harding AK, Lai D (2006) Physics of strongly magnetized neutron stars. Rep Prog Phys 69(9):2631–2708. https://doi.org/10.1088/0034-4885/69/9/R03

Appendix B
Pulsar Timing

When analyzing pulsar data one has to take into account that the times of arrival (TOAs) of the pulses at the observatory on Earth, do not directly reflect the timing of the pulsed emission at the pulsar site. A general relativistic frame transformation between observatory proper time and pulsar proper time is necessary to compute the *pulse phase* of the emission via a model of the intrinsic variations in the pulse period. Pulse phases are usually given in the range of [0, 1[or [0, 360[corresponding to a full rotation of the neutron star.[2] In the following we will roughly sketch out how to compute pulse phases. For an comprehensive introduction to pulsar timing the reader is referred to the excellent descriptions by [1, 2].

Inertial Reference Frame

The center of mass of the solar system, known as Solar system barycentre (SSB), moves essentially uniformly through space and is therefore a convenient inertial frame of reference. It is common to transform the observed TOA, $t_{\rm obs}$, to an equivalent TOA for the same pulse wave-front at the SSB, which requires the quantitative calculation of a numerous of time delays originating from geometrical, relativistic and dispersion effects. The propagation delay from the pulsar to the SSB is usually ignored, but orbital motions of the pulsar, if present, must indeed be taken into account. Considering the most significant ones, we obtain following expression for the time of emission (for a complete discussion of all the time delays, the reader is referred to [2]):

$$t_e = t_{\rm obs} - \triangle_C - \triangle_{R\odot} - \triangle_{E\odot} - \triangle_{S\odot} - \triangle_D - \triangle_B, \tag{B.1}$$

[2]It is common practice, however, to show two rotations in the pulsar light curves for clarity.

D. Carreto Fidalgo, *Revealing the Most Energetic Light from Pulsars and Their Nebulae*, Springer Theses, https://doi.org/10.1007/978-3-030-24194-0

where (typical values for the delays are given in brackets, taken from Hobbs et al. [1]):

- $\triangle_{\mathbf{C}}$ [$\sim$1 μs]: The *Clock delay* takes into account that the TOAs are measured against a local clock at the observatory. Usually these measurements are transformed to a relativistic dynamical time scale such as TDB (Barycentric Dynamical Time) or TCB (Barycentric Coordinate Time).
- $\triangle_{\mathbf{R}\odot}$ [$\sim$500 s]: The *Roemer delay* is the vacuum delay between the arrival of the pulse at the observatory and the Solar system barycenter. Normally the distance from the observatory to the pulsar is much bigger than the distance to the SSB ($|\mathbf{r}_{\mathrm{op}}| \gg |\mathbf{r}_0|$, see Fig. B.1) and the curvature of the wave-front connecting photons simultaneously emitted from the pulsar can be neglected.
- $\triangle_{\mathbf{E}\odot}$ [$\sim$1.6 ms]: The *Einstein delay* is due to the relativistic space-time transformation of the coordinate frame of the observatory to the quasi-inertial frame of the Solar system barycenter. While the relativistic length contraction is negligible, the time dilation is not.
- $\triangle_{\mathbf{S}\odot}$ [$\sim$112 μs]: The *Shapiro delay* accounts for the time delay caused by the passage of the pulse through curved space-time and is obtained considering all the bodies in the Solar system.
- $\triangle_{\mathbf{D}}$: The dispersion delay affects primarily radio signals that encounter significant dispersion in the interplanetary (Solar wind) as well as in the interstellar medium. Since this delay is inversely proportional to the frequency of the observed photon ($\triangle_{D\odot} \propto \nu^{-2}$), in the case of gamma rays this term is neglected.
- $\triangle_{\mathbf{B}}$: Especially millisecond pulsars are often found in binary systems. This term takes into account any orbital motion of the pulsar as well as further effects of the companion, such as an Einstein delay and a Shapiro delay.

Modeling the Pulse Phase

After relating a measured TOA to a time of emission, one now can try to model the intrinsic variations in the pulse period. A basic characteristic of a pulsar is the precise period P modulated by a slow increase due to a gradual loss of rotational energy ($\mathrm{d}P/\mathrm{d}t \simeq 10^{-15}$). In most cases a Taylor expansion with two or three terms is sufficient to predict accurately enough the pulse phase ϕ (see [2]):

$$\phi(t) = \sum_{n\geq 1} \frac{\nu^{n-1}}{n!} (t_e - t_P)^n + \phi_0, \tag{B.2}$$

where $[\nu^{n-1}]$ are the frequency derivative terms and our fit parameters, while t_P is the epoch in which $\dot{\phi} = \nu$ and is set by the user. ϕ_0 is introduced to achieve absolute phase alignment and is normally defined in terms of a reference TOA for a specific observing site and frequency. The fractional part of ϕ is then used to assign pulse

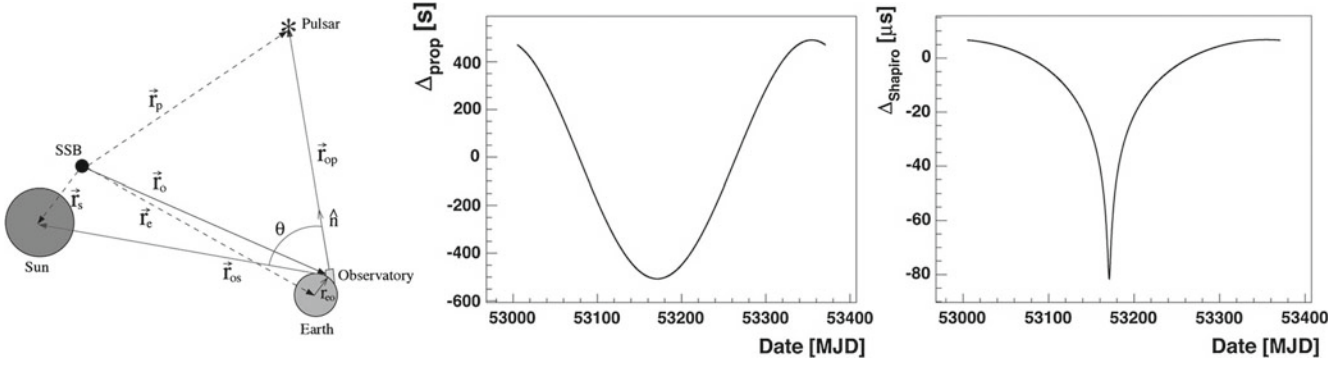

Fig. B.1 **Left**: Sketch of the *Roemer delay*. $|\mathbf{r}_{op}|$ is assumed to be much bigger than $|\mathbf{r}_0|$. **Middle:** The Roemer delay as a function of time. The delay is plotted over a time span of one year. **Right:** The *Shapiro delay* as a function of time. Figures adopted from [3]

phases to observed events. One way to fit Eq. B.2 to our TOAs $t_{e,i}$ is to define a priori a pulse phase model ϕ_a with an approximate frequency (by means of, for example, the Fourier transform) and minimize the residuals $\phi_a(t_{e,i}) - N_i$, where N_i is the nearest integer to $\phi_a(t_{e,i})$. This is normally an iterative procedure in which ϕ_a gets updated with the post-fit parameters.

The set of parameters in Eq. B.2 form a basic *ephemeris* of the pulsar, which can be arbitrarily expanded with further parameters reflecting a more complex timing model. With a given pulsar ephemeris we can assign pulse phases to our events and *phase fold* them to obtain pulsar light curves, also referred to as *phaseograms*. Phase folding consists of binning the data with respect to their assigned pulse phases.

Timing Irregularities

Although pulsars show a remarkable precision in its rotation, there are random irregularities in the periods that are measured as phase deviations in the pulses' TOAs. This *timing noise* is often given as the root-mean-square (RMS) of the residuals between the measured and predicted TOAs. Especially young pulsars exhibit large timing noise of up to $\sim$1 s, whereas millisecond pulsars rotate far more stable ($\sim$1 μs, see [4]). Pulsar timing noise can usually be subdivided into a *white* component (equal power at all fluctuation frequencies) and a *red* component (greater power at lower fluctuation frequencies). A proper characterization of the timing noise can mitigate its affect on other parameters of the timing model, such as the timing position of the pulsar, and is therefore desirable when aiming for high precision ephemerides [5].

In contrast to the continuously erratic behavior of the timing noise, pulsars can also show pronounced step changes in rotation speed, known as *glitches*. These events, resulting in a short decrease of the pulsar's period, are rare and one third of those observed took place in the young pulsars Crab and Vela.[3] A possible origin of these sudden spin-ups are thought to be so-called *starquakes*, where the slow down of the pulsar decreases the centrifugal force on the stellar's surface and an abrupt crack of the neutron star's crust changes the pulsar's moment of inertia [6]. While on average a pulsar with a characteristic time τ_c [kyr] will glitch a maximum of $(6 \pm 2) \times \tau_c^{-0.48}$ times per year [7], the Crab pulsar shows an average glitch rate of about $\sim$1 per year.

References

1. Hobbs GB et al (2006) TEMPO2, a new pulsar-timing package - I. An overview. Mon Not R Astron Soc 369(2):655–672. https://doi.org/10.1111/j.1365-2966.2006.10302.x
2. Edwards RT et al (2006) TEMPO2, a new pulsar timing package - II. The timing model and precision estimates. Mon Not R Astron Soc 372(4):1549–1574. https://doi.org/10.1111/j.1365-2966.2006.10870.x

[3] A table of observed glitches from the Crab Pulsar can be found at: http://www.jb.man.ac.uk/pulsar/glitches/gTable.html, last accessed 07/03/2018.

3. López MM (2006) Astronomíia Gamma con el Telescopio MAGIC: Observaciones de la Nebulosa y Pulsar del Cangrejo. PhD thesis
4. Shannon RM, Cordes JM (2010) Assessing the role of spin noise in the precision timing of millisecond pulsars. Astrophys J 725(2):1607–1619. https://doi.org/10.1088/0004-637X/725/2/1607
5. Kerr M et al (2015) Timing gamma-ray pulsars with the fermi large area telescope: timing noise and astronometry. Astrophys J 814(2):128. https://doi.org/10.1088/0004-637X/814/2/128
6. Lattimer JM, Prakash M (2004) The physics of neutron stars. Science 304(5670):536–542. https://doi.org/10.1126/science.1090720
7. Espinoza CM et al (2011) A study of 315 glitches in the rotation of 102 pulsars. Mon Not R Astron Soc 414(2):1679–1704. https://doi.org/10.1111/j.1365-2966.2011.18503.x

Appendix C
The On-Site Analysis Chain of MAGIC

This appendix describes an up-to-date status of the *On-Site Analysis* (OSA) chain operating at the MAGIC site (see Sect. 3.3) and was presented at the ICRC 2015 in form of a poster contribution [1]. As one of the persons in charge of OSA, the author of this thesis continuously worked on it during the course of his Ph.D. studies improving and maintaining its workflow.

The fast processing of the data at the observation site plays an essential part in the operation of the telescopes. OSA provides provisional intermediate-level analysis products that allow for a fast offline analysis, and thus a quick assessment of the nights data in the case of targets of opportunity like flaring sources. Moreover, the members of the MAGIC collaboration normally use the low-level analysis products provided by OSA for their scientific analyses.

OSA has steadily improved since the beginning of the experiment and we present here the status of the system, including the latest upgrades and details on its performance. The first section provides an overview of the computing infrastructure available at the MAGIC site and the organization of the data flow across the different systems. The second section is devoted to OSA's pipeline, its workflow and the performance.

Computing Infrastructure and Data Flow

The computing system at the MAGIC site consists of a cluster of computers linked by internal networks and accessible from outside via a public web server.[4] Data Acquisiton (DAQ) and operations are carried out in the DAQ and subsystem servers, while data processing takes place in the analysis cluster. The later is composed of a set of high performance computing (HPC) servers running the same operating system (Scientific Linux Cern 6.3) and sharing both network and disk access. The storage capacity of the whole cluster is provided by four RAID systems and local disks

[4] http://www.magic.iac.es/, last accessed 19/04/2018.

D. Carreto Fidalgo, *Revealing the Most Energetic Light from Pulsars and Their Nebulae*, Springer Theses, https://doi.org/10.1007/978-3-030-24194-0

for temporary storage. Each RAID system has a different capacity, configuration and purpose. Volumes devoted to DAQ (RAID1 and RAID2 for the two MAGIC telescopes M1 and M2, respectively), use the XFS file system and are handled by the DAQ machines. Shared volumes (RAID3 and RAID4) store the compressed raw data, software and user data. They are connected by means of a fibre-channel dedicated network, and use a GFS2-formatted file system accessible to every machine of the cluster. The decoupling of the two storage arrays is important since it allows the on-site activities (like the on-site analysis and the data check) to act independently from the data acquisition and to maintain legacy systems used by the DAQ machines isolated from the more modern analysis cluster. Data created at the telescopes (∼100 GB per telescope per hour of observation) are processed in a well-defined chain, comprising different activities according to the logical actions and subsystems involved. The responsibility for each activity relies in a different institute belonging to the MAGIC collaboration, which takes care of the full development and deployment of the services and tools required for a correct processing. The data flow of the activities carried out on-site is sketched in Fig. C.1.

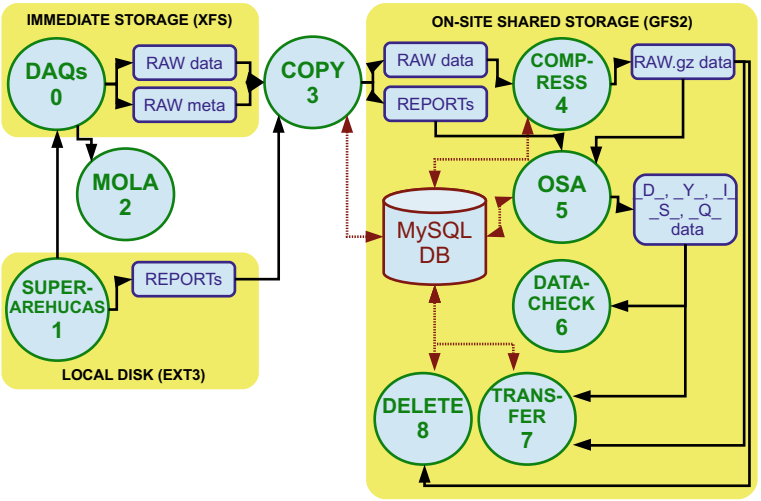

Fig. C.1 Data flow scheme at the MAGIC site. SuperArehucas (1) is the central control for the MAGIC telescopes, controlling the data taking and merging the information of all important subsystems into report files. The copy/compress activities (3, 4) are done simultaneously, while the others follow approximately the sequential order indicated by the number inside the circle. The output of the on-site analysis (5) are low-level analysis products with different key names (*_D_*, *_Y_* etc.). The transfer of the data to the MAGIC data center (7) and the deletion (8) are triggered by the MySQL database that keeps track of the daily activities on-site. For more details on the two processes MOLA and DataCheck the reader is referred to [1, 2]. Image courtesy of Alejandro Lorca

The On-Site Analysis

The aim of OSA is to provide low and intermediate level analysis products to the collaboration on the day after the observation night. OSA essentially takes care of the calibration of the data, the cleaning and parameterization of the images and merges the data from the two MAGIC telescopes. Those steps reduce the file sizes by a factor of ∼200 compared to the compressed raw data and are performed in parallel with the raw data transfer to the MAGIC data center located at the *Port d'Informació Científica* (PIC) in Barcelona. OSA consists of the MAGIC *Analysis and Reconstruction Software* (MARS, [3]), a set of python scripts, Unix cron jobs and a PBS/Torque resource manager to allow for a high degree of parallelization using the 40 cores assigned to OSA in the computer cluster at the MAGIC site. Its objective is achieved by a high degree of parallelization when processing the data and by starting its operation already during the observation night.

OSA and MARS

MARS is a set of C++ classes based on the well known ROOT package from CERN[5] and allows the analysis of MAGIC data by means of compiled programs called MARS executables. OSA interacts with those executables via sub-processes, which are spawned within the python scripts, passing them arguments and evaluating their return codes. The main MARS executables used by OSA are the following:

- *sorcerer*: takes as input the compressed raw data and calibrates it.
- *merpp*: adds the central control reports to the calibrated files.
- *star*: performs the cleaning and the parametrization of the images.
- *superstar*: combines the M1 and M2 *star* files, containing image parameters, and performs the stereo reconstruction.
- *melibea*: estimates the event properties, for example energy, direction and particle kind.

In general, collaboration members start their analyses with *star* or *superstar* files provided by OSA since the next step (*melibea*) requires input generated with the help of Monte Carlo simulations, which on the other hand depend on the instrument setup and analysis goals. Another reason is that OSA does not make any kind of data selection regarding the quality of the data. This is usually done by the analyzer at the *star* or *superstar* level. *Melibea* files are produced to allow for a quick but preliminary off-line analysis of targets of opportunity.

[5] https://root.cern.ch, last accessed 28/02/2018.

OSA Workflow

Every hour, the copy/compress process (see Fig. C.1) looks for new raw data on the immediate (DAQ) storage and copies it together with the corresponding report files to the on-site shared storage, classifying it by observation nights. With the same frequency and after a short delay, the on-site analysis chain is initiated by cron jobs that execute the so-called *sequencer* (see Fig. C.2). This script, with the help of the *nightsummary* script, checks for available raw data in the shared storage system and gathers information from the report files for a given observation night. The *sequencer* then goes on to create a list of sequences to be analyzed, establishes relationships between them, making the execution of some of them dependent on the successful completion of others, and sends them to the Torque queue system. Three types of sequences are built, depending on the content of the input files:

- *Calibration*: to process the calibration runs taken for each source before starting the observation.
- *Data*: to process a data run of one telescope, which by default have an observation time of 20 min.
- *Stereo*: to merge and process the output files of the *Data* sequences for each telescope sharing the same data run.

While the command line arguments `M1` and `M2` build *Calibration* and *Data* sequences for the corresponding telescope, `ST` results in a list of *Stereo* sequences. The sequences are processed in the working nodes of the computer cluster and handled by different scripts according to their type (*calibrationsequence*, *littlesequence* and *stereosequence*, respectively). The Torque system balances the charge among the nodes.

The standard output of the *sequencer* is a human readable table displaying the characteristics, status and progress of each sequence. This table is automatically

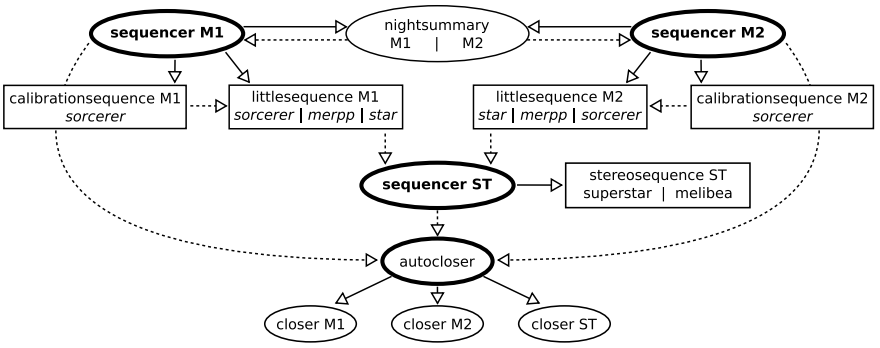

Fig. C.2 A sketch of the OSA workflow. Ellipses indicate scripts run in the user interface (bold ones are initiated be cron jobs) while scripts inside boxes are executed anywhere in one of the working nodes. Solid lines represent job submissions or process calls while dashed lines illustrate dependencies. The MARS executables called by the respective python scripts are written in italic

interpreted by the *autocloser* script that is executed by a cron job on the half-hour. When it detects that the analysis has finished for all the sequences of `M1`, `M2` or `ST`, the *autocloser* calls the *closer* script. This *closes the day* for the corresponding data (`M1`, `M2`, or `ST`), triggering the transfer of the respective analysis products to the MAGIC data center through an entry in the MySQL database. The output of the sequencer is also copied periodically to a web page for visual inspection by the OSA team.

OSA Performance

The first version of OSA was installed in 2005 and consisted of a small set of shell scripts called by cron jobs. Since then it underwent several updates/changes with a significant remodeling during 2012 when the whole system was transferred to python and the storage system was separated into the immediate storage and the on-site shared storage system. This decoupling allows OSA to start the analysis chain already during the night after the first data is available without disturbing the rest of the data taking.

At the end of 2014, a change in the *nightsummary* script and some helper modules permitted the automatic analysis of some non-standard observations. Additionally, the introduction of the *autocloser* script, developed by the author of this thesis, automatized the interpretation of the *sequencer* table and the *closing of the day*, tasks that formerly had to be taken care of manually. Both modifications led to a higher degree of automatization and significantly decreased the workload for the OSA staff.

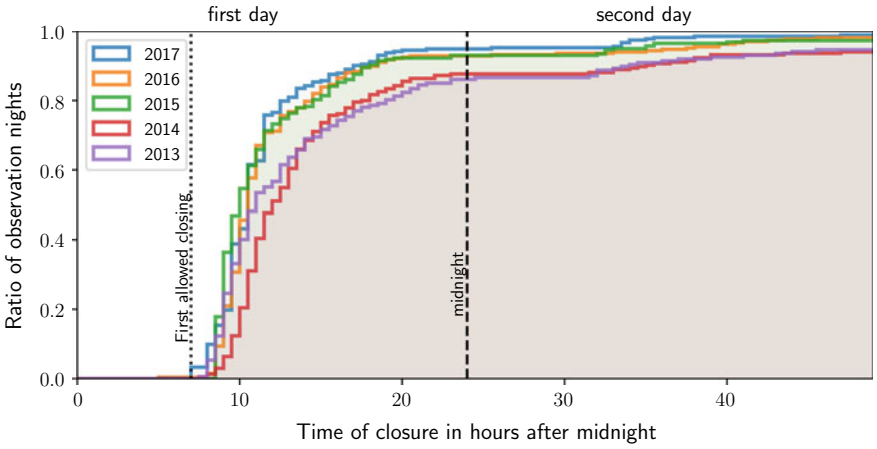

Fig. C.3 OSA performance for closing the stereo analysis (`ST`) for the last 5 years of operation. The *y*-axis shows the ratio of nights closed before $\times$ hours after midnight. Statistics could only be gathered from 2013 on. Image courtesy of Mireia Nievas-Rosillo (Color figure online)

The performance of OSA over the last 5 years measured by the time needed to process the data of a single day is shown in Fig. C.3. As for 2017, OSA completes the analysis of `M1` and `M2` for ∼85% of the observation nights within the first 12 h after midnight, while for the stereo analysis it is ∼80%. About 95% of the observation nights are completely analyzed and closed within the first 24 h. For the rest of the nights, OSA encounters major problems that require a deeper intervention by the OSA staff and are normally fixed within three days.

Together with a stable transfer of the analysis products to the MAGIC data center, where it becomes accessible to the general collaboration, OSA provides the possibility of a fast offline analysis and therefore allows for an adaptive scheduling of targets of opportunity like flaring sources.

References

1. Fidalgo D et al (2015) Data processing activities at the MAGIC site. In: 34th international cosmic ray conference, The Hague, Netherlands, p 8
2. Tescaro D et al (2013) The MAGIC telescopes DAQ software and the on-the-fly online analysis client. In: 33rd international cosmic ray conference, Rio de Janeiro, Brazil, pp 2–5
3. Zanin R et al (2013) MARS, the MAGIC analysis and reconstruction software. In: 33rd international cosmic ray conference, Rio de Janeiro, Brazil, p id 773

Appendix D
Details on the Crab Pulsar Analysis

This appendix provides some further details on the analysis of the Crab pulsar presented in Chap. 5. The individual sections correspond to references made in the main text of Chap. 5.

Cleaning Methods and Cleaning Levels

The image cleaning parameters reflect to a certain extent the hardware configuration of the telescopes at the time (see Sect. 3.3 for an overview of the hardware changes). Table D.1 summarizes the image cleaning methods and cleaning levels that were applied to our subsamples. The amount of work that would be involved in the reprocessing of the archival data with the advanced *sum* cleaning algorithm, is out of scope for this thesis. In addition, the *sum* cleaning hardly improves MAGIC's performance in the energy range above 400 GeV, and hence should not affect our study of the most energetic radiation emitted by the Crab pulsar.

Table D.1 Cleaning method and cleaning levels for the different subsamples

Analysis period	Cleaning method	Cleaning levels [Lvl1/Lvl2]	
		M1	M2
M1 *	Absolute	6/3	–
ST.01.02 (On/Off)	Absolute	6/3	9/4.5
ST.01.02 (Wobble)	Sum	4/3	7/4
≥ST.02.01	Sum	6/3.5	6/3.5

Notes For a description of the cleaning methods, see Sect. 3.4. No distinction was made with respect to the zenith angles in each analysis period. The analysis period ST.01.02 belongs to the time span in which MAGIC operated with two different cameras in MAGIC-I and II, and two different readouts (see Sect. 3.3). For ST.01.02 (Wobble) the levels were optimized by Gianluca Giavitto

D. Carreto Fidalgo, *Revealing the Most Energetic Light from Pulsars and Their Nebulae*, Springer Theses, https://doi.org/10.1007/978-3-030-24194-0

Pulsar Light Curve Fitting

For the fitting of the phaseogram we define a probability density function (PDF) for the phase ϕ of our events. The PDF includes the two peaks plus a constant in phase accounting for the background, and hence reads:

$$\mathrm{PDF}(\phi \mid P1, \boldsymbol{\nu_1}, P2, \boldsymbol{\nu_2}, B) = \frac{P1\, p(\phi, \boldsymbol{\nu_1}) + P2\, p(\phi, \boldsymbol{\nu_2}) + B}{P1 + P2 + B}, \tag{D.1}$$

where $P1$, $P2$ and B are the intensities of the main pulse, the inter-pulse and the background, respectively. $\boldsymbol{\nu_1}$ and $\boldsymbol{\nu_2}$ are the model parameters for the peak shape p, which we model with three different normalized functions:

- a Gaussian:
$$p(\phi, \mu, \sigma) = \frac{1}{\sqrt{2\pi}\sigma}\ \exp[-\frac{(\phi-\mu)^2}{2\sigma^2}] \tag{D.2}$$

- an asymmetric Gaussian:
$$p(\phi, \mu, \sigma_1, \sigma_2) = \frac{2}{\sqrt{2\pi}(\sigma_1+\sigma_2)} \begin{cases} \exp[-\frac{(\phi-\mu)^2}{2\sigma_1^2}], & \phi < \mu \\ \exp[-\frac{(\phi-\mu)^2}{2\sigma_2^2}], & \phi > \mu \end{cases} \tag{D.3}$$

- and a Lorentz function:
$$p(\phi, \mu, \gamma) = \frac{1}{\pi\gamma}\ \frac{\gamma^2}{(\phi-\mu)^2+\gamma^2}. \tag{D.4}$$

With the PDF at hand we compute the likelihood function

$$\mathcal{L}\left(P1, \boldsymbol{\nu_1}, P2, \boldsymbol{\nu_2}, B \mid \{\phi_i\}_{i=0}^{N}\right) = \prod_{i=0}^{N} \mathrm{PDF}(\phi_i \mid P1, \boldsymbol{\nu_1}, P2, \boldsymbol{\nu_2}, B), \tag{D.5}$$

where N is the total number of events in our light curve. To obtain our model parameters, we minimize the negative logarithmic of $\mathcal{L}$ using the *iminuit* package[6] for python, which is based on the Minuit algorithm by James and Roos [1]. In the case of comparing nested models (for example a symmetric and an asymmetric Gaussian peak shape), we use the *likelihood ratio test* for which the probability distribution of its test statistics can be approximated following [2].

[6] iminuit – A Python interface to Minuit. https://github.com/iminuit/iminuit.

Spillover in the >400 GeV Pulsar Light Curve

Due to the finite energy resolution of the instrument, we inevitably will get some spillover of events with a true energy below 400 GeV that cannot be corrected for on an event-by-event basis in our pulsar light curves. Here we try to estimate the percentage of gamma-rays in our >400 GeV light curve, which originate from the inter-pulse of the Crab pulsar and have a true energy below 400 GeV. For this estimation we take our MC events with an estimated energy above 400 GeV and check the percentage of events with a true energy below 400 GeV, after reweighing the distribution to mimic the spectrum of the inter-pulse of the Crab pulsar (that is a power-law spectrum of -3.13). This exercise is done for each subsample of our data set and the resulting percentages are weighted by the number of excess events found in the corresponding subsample (if the number of excess events is negative, we discard the subsample from our estimation). The final number is then the weighted average of the percentages resulting in an estimated spillover of $15.8 \pm 0.4\%$. The error is estimated by applying a bootstrap method in which we draw the weights from a Gaussian distribution centered on the number of excess events and a standard deviation equal to the error of the excess events. The stated error is then the standard deviation of the obtained distribution of averaged spillovers.

Spectral Points

In Table D.2 we provide the numerical values to the spectral points derived in Fig. 5.8. The spectral points were unfolded by means of the Bertero method for the regularization (see Sect. 3.4), and thus the statistical errors are correlated. The covariance matrices for the two spectra, the main pulse P1 and the inter-pulse P2, respectively, are given on the next page.

The covariance matrix for the spectral points in Fig. 5.8. Matrix D.6 and D.7 belong to the main pulse P1 and the inter-pulse P2, respectively.

$$\begin{bmatrix} 1.59e^{-22} & 1.46e^{-23} & -1.19e^{-24} & -2.02e^{-25} & -1.19e^{-26} \\ 1.46e^{-23} & 1.22e^{-23} & 2.14e^{-24} & -6.95e^{-26} & -2.26e^{-26} \\ -1.19e^{-24} & 2.14e^{-24} & 1.67e^{-24} & 2.18e^{-25} & -1.37e^{-26} \\ -2.02e^{-25} & -6.95e^{-26} & 2.18e^{-25} & 2.11e^{-25} & 2.59e^{-26} \\ -1.19e^{-26} & -2.26e^{-26} & -1.37e^{-26} & 2.59e^{-26} & 2.60e^{-26} \end{bmatrix} \tag{D.6}$$

Table D.2 Fluxes and numerical values for the spectral points in Fig. 5.8

Energy bin (GeV)	Main pulse (P1) $\frac{\mathrm{d}N}{\mathrm{d}E}$ ($\mathrm{cm}^{-2}\ \mathrm{s}^{-1}\ \mathrm{TeV}^{-1}$)	Inter-pulse (P2) $\frac{\mathrm{d}N}{\mathrm{d}E}$ ($\mathrm{cm}^{-2}\ \mathrm{s}^{-1}\ \mathrm{TeV}^{-1}$)
69–108	$(0.70 \pm 0.13) \times 10^{-10}$	$(1.48 \pm 0.14) \times 10^{-10}$
108–167	$(1.17 \pm 0.35) \times 10^{-11}$	$(2.77 \pm 0.38) \times 10^{-11}$
167–259	$(0.31 \pm 0.13) \times 10^{-11}$	$(0.60 \pm 0.14) \times 10^{-11}$
259–402	$(1.02 \pm 0.46) \times 10^{-12}$	$(2.15 \pm 0.49) \times 10^{-12}$
402–623	$(0.24 \pm 0.16) \times 10^{-12}$	$(0.73 \pm 0.18) \times 10^{-12}$
623–965	–	$(1.68 \pm 0.72) \times 10^{-13}$
965–1497	–	$(0.63 \pm 0.29) \times 10^{-13}$
(GeV)	$E^2 \frac{\mathrm{d}N}{\mathrm{d}E}$ ($\mathrm{TeV\ cm}^{-2}\ \mathrm{s}^{-1}$)	$E^2 \frac{\mathrm{d}N}{\mathrm{d}E}$ ($\mathrm{TeV\ cm}^{-2}\ \mathrm{s}^{-1}$)
69–108	$(5.00 \pm 0.90) \times 10^{-13}$	$(1.07 \pm 0.10) \times 10^{-12}$
108–167	$(2.02 \pm 0.60) \times 10^{-13}$	$(4.80 \pm 0.65) \times 10^{-13}$
167–259	$(1.28 \pm 0.53) \times 10^{-13}$	$(2.48 \pm 0.57) \times 10^{-13}$
259–402	$(1.01 \pm 0.46) \times 10^{-13}$	$(2.15 \pm 0.49) \times 10^{-13}$
402–623	$(0.56 \pm 0.38) \times 10^{-13}$	$(1.75 \pm 0.44) \times 10^{-13}$
623–965	–	$(0.97 \pm 0.41) \times 10^{-13}$
965–1497	–	$(0.88 \pm 0.41) \times 10^{-13}$

Notes The energy values of the spectral points are chosen such, that the resulting spectral function at these energies is the same as its average in the corresponding energy bin. The resulting spectral functions are given in Table 5.4

$$\begin{bmatrix} 1.94e^{-22} & 1.66e^{-23} & -1.51e^{-24} & -2.39e^{-25} & -1.08e^{-26} & -4.44e^{-28} & -3.01e^{-28} \\ 1.66e^{-23} & 1.41e^{-23} & 2.39e^{-24} & -9.90e^{-26} & -2.34e^{-26} & -1.17e^{-27} & -1.26e^{-28} \\ -1.51e^{-24} & 2.39e^{-24} & 1.89e^{-24} & 2.39e^{-25} & -1.45e^{-26} & -2.60e^{-27} & -2.13e^{-28} \\ -2.39e^{-25} & -9.90e^{-26} & 2.39e^{-25} & 2.42e^{-25} & 2.97e^{-26} & -2.14e^{-27} & -3.65e^{-28} \\ -1.08e^{-26} & -2.34e^{-26} & -1.45e^{-26} & 2.97e^{-26} & 3.36e^{-26} & 4.24e^{-27} & -3.60e^{-28} \\ -4.44e^{-28} & -1.17e^{-27} & -2.60e^{-27} & -2.14e^{-27} & 4.24e^{-27} & 5.20e^{-27} & 6.47e^{-28} \\ -3.01e^{-28} & -1.26e^{-28} & -2.13e^{-28} & -3.65e^{-28} & -3.60e^{-28} & 6.47e^{-28} & 8.55e^{-28} \end{bmatrix} \tag{D.7}$$

References

1. James F, Roos M (1975) Minuit - a system for function minimization and analysis of the parameter errors and correlations. Comput Phys Commun 10(6):343–367. https://doi.org/10.1016/0010-4655(75)90039-9.
2. Wilks SS (1938) The large-sample distribution of the likelihood ratio for testing composite hypotheses. Ann Math Stat 9(1):60–62. https://doi.org/10.1214/aoms/1177732360

Index

D. Carreto Fidalgo, *Revealing the Most Energetic Light from Pulsars and Their Nebulae*, Springer Theses, https://doi.org/10.1007/978-3-030-24194-0